REFERENCES

1. E. M. Epperlein, G. J. Rickard, and A. R. Bell, *Phys. Rev. Lett.* **61**, 2453 (1988); *Comput. Phys. Commun.* **52**, 7 (1988); E. M. Epperlein and R. W. Short, *Phys. Fluids B* **3**, 3092 (1991); **4**, 2211 (1992).

2. E. M. Epperlein, "Fokker-Planck Modeling of Electron Transport in Laser-Produced Plasmas" (to be published in *Laser and Particle Beams*).

3. J. S. Chang and G. Cooper, *J. Comput. Phys.* **6**, 1 (1970).

4. E. W. Larsen, C. D. Levermore, G. C. Pomraning, and J. G. Sanderson, *J. Comput. Phys.* **61**, 359 (1985).

5. A. B. Langdon, in *CECAM Report of Workshop on "The Flux Limiter and Heat Flow Instabilities in Laser-Fusion Plasmas"* (Universite Paris Sud, France, 1981), p. 69.

6. T. H. Kho, *Phys. Rev. A* **32**, 666 (1985).

7. Y. A. Berezin, V. N. Khudick, and M. S. Pekker, *J. Comput. Phys.* **69**, 163 (1987).

8. I. P. Shkarofsky, *Can. J. Phys.* **41**, 1753 (1963).

9. W. R. Briley and H. McDonald, *J. Comput. Phys.* **34**, 55 (1980).

10. J. R. Albritton, *Phys. Rev. Lett.* **50**, 2078 (1983).

11. L. Spitzer, Jr. and R. Härm, *Phys. Rev.* **89**, 977 (1953).

12. S. G. Glendenning *et al.*, *Phys. Rev. Lett.* **69**, 1201 (1992).

1.B   New Diagnostic Features in the Spectra of Recent Argon-Filled-Target Implosions on OMEGA

Recent argon-filled-target implosions were performed for two kinds of target fills: (a) low-pressure argon in an Ar-DD mixture and (b) high-pressure argon. These experiments provide additional diagnostic signatures for comparison to code predictions. Generally, the measurements indicate deviations from predictions and can serve as indirect evidence of instability.

Targets of low argon-fill pressure have the distinction of low opacity of argon lines. This means that the observed line emission can yield information on the peak core conditions. In addition, we observe the free-bound continuum, which in high-pressure shots is indistinct due to opacity effects. This spectral feature provides additional information on the core electron temperature (through the continuum slope as well as the continuum jump) and on the core density (through the reduction in ionization energy).

Targets with high argon-fill pressure provide information on the cooler, peripheral argon layer of the core through the observation of absorption lines. In the past, absorption lines of 1s–2p transitions in argon ions with a partially filled L shell have been observed. Here, we also observe 1s–3p transitions in absorption. These lines provide information on the temperature and $\rho\Delta R$ of that cooler region. However, the predicted strong absorption of helium-like argon lines has not been observed. This is interpreted as due to a cooler-than-predicted compressed core.

Table 55.I lists the experimental conditions for the shots used in the analysis. All targets were polymer shells, overcoated with a 0.05-μm layer of Al (to protect against shinethrough), imploded by 600-ps OMEGA pulses. These shots were also part of an NLUF experiment performed by C. F. Hooper and colleagues from the University of Florida.

Table 55.I: Experimental conditions for the shots used in the analysis.

Shot No.	Target Diameter (μm)	Target Thickness (μm)	Fill Pressure		Laser Energy (J)
			DD (atm)	Ar (atm)	
24501	254	6	20	0.1	943
24498	248	6	0	20	976

Low-Pressure Argon Experiments

Figure 55.8 shows the spectrum for shot 24501, emitted by a low-argon-pressure target. The argon lines are generally of low opacity for such low argon-fill pressure. We can predict this low opacity even without knowing the degree of target compression. To see that, we note that the opacity of a layer of areal density $\rho\Delta R$ due to resonant line absorption is given by $\tau_\nu = \left(\pi e^2 f / M_i mc\right)\rho\Delta R\, b\, P(\nu)$, where τ_ν is the opacity at the frequency ν, f is the absorption oscillator strength, b is the fraction of all ions in the absorbing ground state, M_i is the ionic mass, and $P(\nu)$ is the line profile in inverse-frequency units (normalized to unit area) at the frequency ν. For Stark-broadened lines, the line width ΔE is proportional to $\rho^{2/3}$, so that $P(\nu) \sim \rho^{-2/3}$. Strictly speaking, this is only true for the ion-broadening component of the profile; however, for lines like Lyman-β, having no unshifted Stark component (hence, a central dip), this is practically true for the total profile. Since for a given target implosion $\rho R = (3M / 4\pi)^{1/3}\,\rho^{2/3}$, where M is the total argon mass, the line-center opacity depends only on the initial fill mass (or the fill pressure and radius) but not on the compression. For the Ar Lyman-β line, the opacity at the two line peaks (straddling the central dip) becomes $\tau_{max} \sim 0.1\, bp^{1/3}R_o$, where p is the fill pressure in atmospheres and R_o the initial radius in microns. For shot 24501, this becomes $\tau_{max} \sim 2$; hence, opacity is small but not negligible.
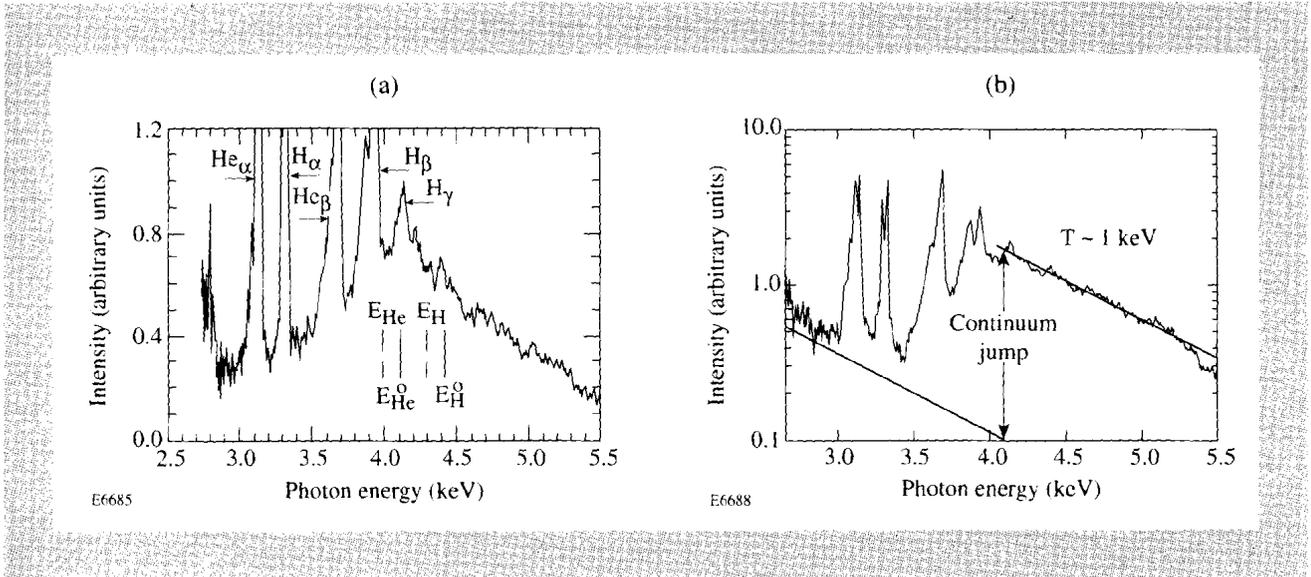
Fig. 55.8

Calibrated spectrum from a low-pressure argon target (shot 24501). The target was filled with a mixture of 0.1 atm argon and 20 atm deuterium. (a) The vertical bars show the unshifted positions of the hydrogen-like and helium-like K edges (o subscript), as well as the shifted positions, calculated from the experimentally determined density and temperature. H and He refer to Ar^{+17} and Ar^{+16}, respectively. (b) Determining the temperature from the continuum slope and a lower bound of the continuum jump (which yields an upper bound on the temperature). The line marking the continuum jump is arbitrarily placed near 4 keV.

We proceed to fitting theoretical Stark profiles calculated by Hooper[1] to the measured Lyman-β profile of shot 24501, shown in Fig. 55.9. Note that these profiles correspond to the case of a very small admixture of argon in an otherwise deuterium plasma, as is the case in shot 24501. These profiles are somewhat narrower than the profiles for a pure argon plasma for the same electron density. For example, the simplified formula for the ion-broadening of hydrogenic lines[2] shows that for a given electron density, the linewidth is proportional to $Z^{1/3}$, where Z is the charge of the plasma ions (the perturbers). Before fitting to profiles of different densities, we show in Fig. 55.9(a) that Stark profiles are relatively insensitive to the temperature. The two Stark profiles shown are for the same electron density ($N_e = 10^{23}$ cm^{-3}), but two different temperatures (200 and 800 eV). For an unknown temperature in the range of 200 to 800 eV, using a profile for an intermediate temperature, the deduced density can be in error of less than ±20%. The Stark profile also depends slightly on the ion temperature (even before the Doppler broadening is folded in), and we used profiles calculated for $T_i = T_e$. Once we select a calculated profile closest to the measured one, final fitting is obtained by stretching or contracting the energy scale and noting that the profile width changes with density approximately like $N_e^{2/3}$. The Doppler broadening was also included in the calculated profiles. To account for the small opacity, we replace the actual profile $P(\Delta E)$ by the expression $1 - \exp[-\tau_{max} P(\Delta E) / P_{max}]$, where P_{max} is the profile value at either peak and $\tau_{max} = 2$, as explained above. The best-fit profile corresponds to an electron density of 0.7×10^{24} cm^{-3}, or $\rho \sim 2.3$ g cm^{-3}. The assumed temperature for the theoretical profile was 1.0 keV, in anticipation of the results obtained below.

The spectrum in Fig. 55.8 provides an additional diagnostic feature, the free-bound continuum. Note that the intensity scale in Fig. 55.8(a) is linear, whereas in Fig. 55.8(b) it is logarithmic. This is the continuum due to recombination into the K shell, and it appears at energies above the K edge. There are two, close K edges here: (a) the Ar^{+17} edge, due to recombination of electrons and Ar^{+18} ions, at 4.426 keV, and (b) the Ar^{+16} edge, due to recombination of electrons and Ar^{+17} ions, at 4.120 keV. First, the electron temperature in the compressed core can be deduced from the slope of the free-bound continuum, which in Fig. 55.8(b) corresponds to $T_e \sim 1.0$ keV. For the slope determination we look beyond the K edge of the first continuum ($e^- + Ar^{+18}$), where the two continua simply add up. As described below, the edge is shifted into lower photon energies, which facilitates the slope measurement.
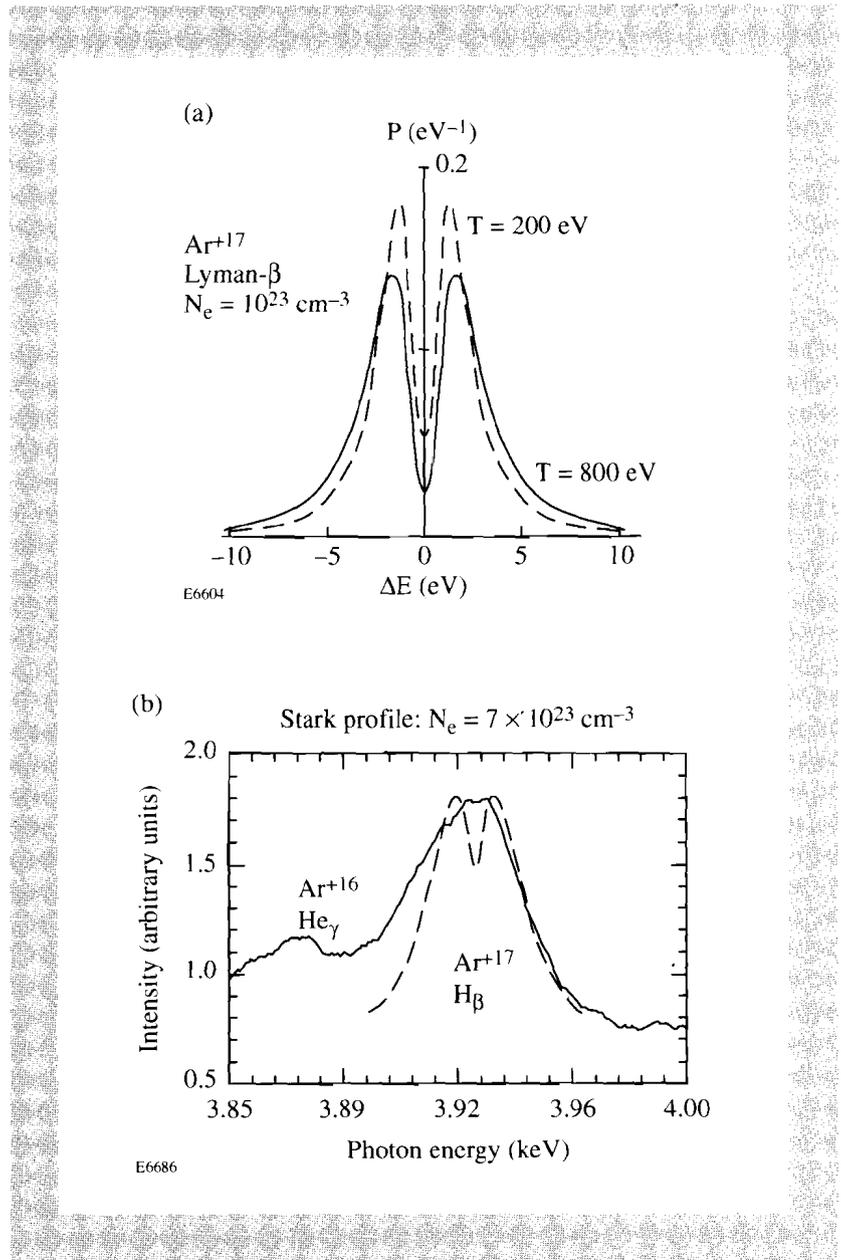

Fig. 55.9
(a) Calculated Stark profiles (from Ref. 1) for the same electron density but two different temperatures. For an unknown temperature in the range of 200 to 800 eV, the deduced density can be in error of less than ±20%. (b) Fitting of a theoretical Stark profile to the measured Lyman-β line of Ar^{+17} (at 3151 eV) for shot 24501.

An additional signature associated with the free-bound continuum is the reduction of ionization energy. As is evident from Fig. 55.8, the free-bound continua extend well into the low-energy side of the K edge before falling. This reduction is due to the interaction with neighboring ions (or the background plasma) and depends on the density and temperature. Because of the overlap of the Ar^{+17} edge with the $e^- + Ar^{+17}$ continuum, it is easier to determine the measured shift of the Ar^{+16} edge. Generally, the effect increases with increasing density and decreasing temperature. Using the theory developed by Stewart and Pyatt,[3] we show in Fig. 55.10 the calculated reduction in ionization energy of helium-like argon (Ar^{+16}) for the relevant parameter ranges. The calculation is for the same argon-to-deuterium ratio as in shot 24501 (1:200 in fill pressures). A similar calculation was done for hydrogen-like argon (Ar^{+17}). As seen, the reduction depends on both temperature and density for the parameter ranges encountered here. There are two limiting expressions (defined by the number N_D of particles in the Debye sphere) that are sometimes used for the reduction in the ionization energy ΔE_i:

$$\Delta E_i = e^2 / r_D \quad \left(\text{for } N_D \gg 1\right)$$

and

$$\Delta E_i = e^2 / a \quad \left(\text{for } N_D \ll 1\right). \tag{1}$$

where r_D is the Debye length and a is the ion-sphere radius; the first is given by the Debye-Huckel theory and the second by the ion-sphere model. As a rule, the Stewart-Pyatt model gives smaller energy shifts than either theory. In addition, the parameter ranges in Fig. 55.10 correspond to intermediate values of N_D ($N_D \sim 1$). As a result, ΔE_i in Fig. 55.10 does depend on the temperature, which is not the case for the ion-sphere model; however, the dependence on density is closer to that of the ion-sphere model ($\sim \rho^{1/3}$) than to that of the Debye-Huckel model ($\sim \rho^{1/2}$).

Using Fig. 55.10, we estimate the reduction in ionization energy in the experiment (shot 24501). We use the density value derived from the Stark broadening of the Lyman-β line [Fig. 55.9(b)], and the temperature derived from the continuum slope [Fig. 55.8(b)]. The derived reduction for Ar^{+16} is $\Delta E_i = 120$ eV, and for Ar^{+17} the reduction is 130 eV. The vertical bars in Fig. 55.8(a) show the unshifted positions of the hydrogen-like and helium-like K edges (o subscript), as well as the shifted positions, calculated from the experimentally determined density and temperature. As seen, the predicted reduction is generally consistent with the shape of the measured continuum. The shift of the hydrogen-like edge is not clearly seen because of a smaller continuum jump at this edge.
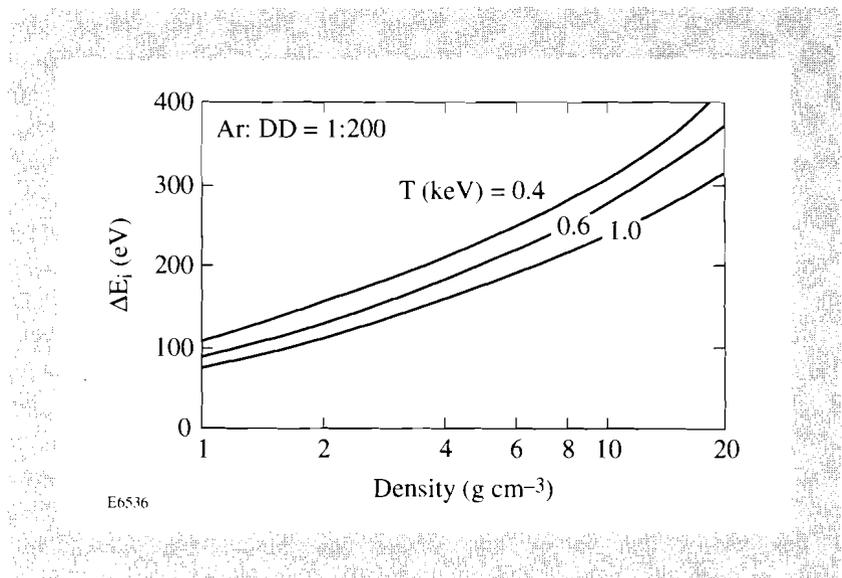
Fig. 55.10
Calculated reduction in ionization energy of Ar^{+16} (helium-like argon) for the relevant parameter ranges, using the theory of Stewart and Pyatt (Ref. 3). The calculation is for the same argon-to-deuterium ratio as in shot 24501 (1:200 in fill pressures).

The electron temperature can be additionally estimated from the continuum jump. This is the intensity ratio (I^+/I^-) between the continuum just to the high-energy side of the K edge and that to the low-energy side. The continuum on the low-energy side is due to recombination to higher levels (L shell, etc.) as well as due to bremsstrahlung. The continuum on the high-energy side of the edge is due to all these processes, in addition to recombination to the K shell. This jump decreases strongly with increasing temperature because recombination radiation at a given frequency varies like $(kT)^{-3/2} \exp\left[(E_i - h\nu)/kT\right]$, whereas bremsstrahlung varies like $(kT)^{-1/2} \exp(-h\nu/kT)$; hence, the ratio of the first to the second varies like $(kT)^{-1} \exp(E_i/kT)$.

Since the dependence of both recombination and bremsstrahlung on electron density is the same ($\sim N_e^2$), one would expect this dependence to cancel out and leave only a temperature dependence. This indeed is the case in a calculated curve of the continuum jump near the K edge of hydrogen-like ions.[4] In that curve, the density-independent continuum jump is monotonically decreasing with increasing temperature. However, we need to modify that curve in two ways. First, the density independence of the continuum jump due to a given species is only correct for a constant fraction of the relevant ion species. The K-edge jump of Ar^{+17} will start to fall as the temperature decreases because recombination $\left(e^- + Ar^{+18} \Rightarrow Ar^{+17}\right)$ will reduce the number of available Ar^{+18} ions. The effect of the varying fraction of Ar^{+18} ions with temperature (which also depends on density) was not included in the calculation of Ref. 4. Thus, instead of one monotonically decreasing curve, the continuum jump as a function of temperature has a maximum at low temperatures, which is density dependent. Only at high enough temperatures do the curves for different densities approach each other. Second, we need to calculate the jump near the Ar^{+16} (helium-like) edge since this jump is much more distinct than that near the

Ar^{+17} edge and is easier to compare to the experiment. For this continuum jump, the curves at high temperature decrease faster with increasing temperature than in the hydrogen-like calculations because here ionization of the type $Ar^{+17} \Rightarrow Ar^{+18} + e^-$ reduces the number of Ar^{+17} ions, just as recombination of the type $\left(e^- + Ar^{+17} \Rightarrow Ar^{+16}\right)$ reduces the jump at low temperatures.

We calculated the continuum emission for each ion species from Ref. 5, coupled with the ionic populations calculated with the collisional-radiative code *POPION*.[6] In Fig. 55.11 we show the calculated continuum jump for the K edge of Ar^{+16}, as a function of temperature, for two electron densities. As seen, the curves indeed have density-dependent maxima and only at sufficiently high temperatures become almost density independent. Using the same procedure, we calculated the jump near the Ar^{+17} edge. For the density and temperature values deduced here, that jump is only about 1.1. This jump is dominated by the ratio of Ar^{+18} to Ar^{+17} ion populations, which is much smaller than 1 for these conditions—the reason why this edge is indistinct in Fig. 55.8.
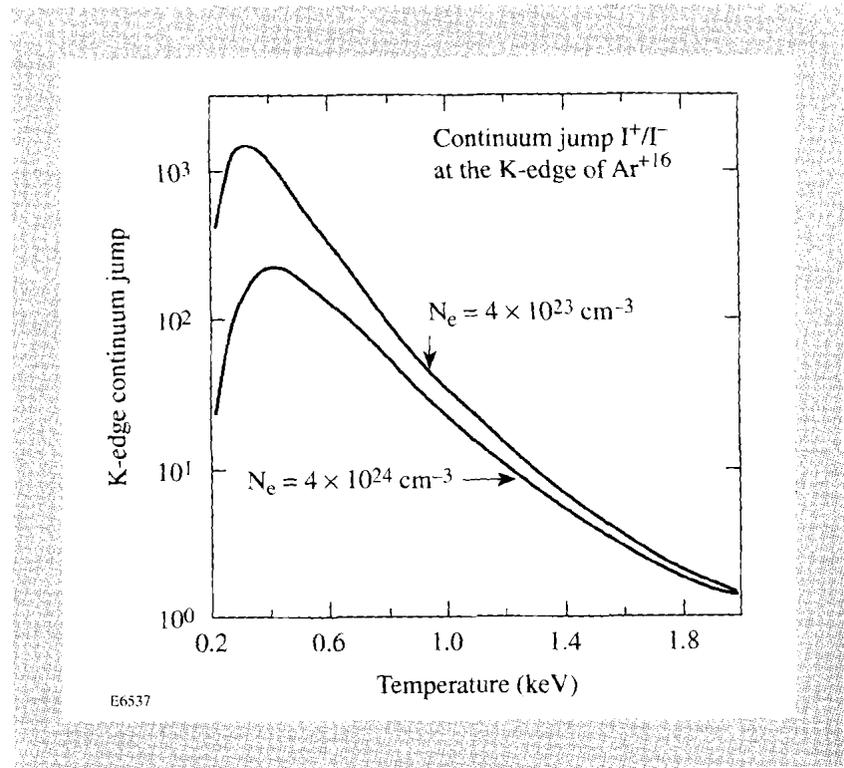

Fig. 55.11
The calculated continuum jump for the K edge of Ar^{+16}, as a function of temperature, for two electron densities.

In Fig. 55.8, only a lower bound on the continuum jump can be estimated because the continuum level on the low-energy side of the edge (I^-) is below the background level. To measure accurately the continuum jump as calculated here, we should have observed a continuum rising from the edge toward lower energies and having the same slope as the continuum above the edge (i.e., corresponding to $T \sim 1$ keV). Such a rising continuum is only seen below ~ 3 keV, and even then it is of a lower temperature. This means that the continuum of ~ 1 keV below the edge is buried underneath the observed background, due to time integration, as well as radiation from, and attenuation by, cooler target regions. To obtain a lower bound on the continuum jump, we draw a line on the

semilog intensity plot [Fig. 55.9(b)] having a slope of 1 keV and going through the lowest observed continuum intensity. This yields a minimum jump of 14, which from Fig. 55.11 corresponds to $T < 1.2$ keV. Note that we have arbitrarily placed the line marking the continuum jump near 4 keV. Because of the high sensitivity of the jump to temperature, only an approximate slope must be known to yield a reasonable temperature estimate.

As an additional diagnostic tool, we use the *RATION* code[7] to calculate the total line and continuum spectrum emitted by an argon plasma of a given temperature and density. *RATION* is a steady-state, non-LTE atomic physics code, which includes the transport of lines through the target using the escape-factor approximation, as well as Stark and Doppler broadening. We vary the temperature and density to achieve best correspondence with the experimental profile. The main value in applying this procedure is to test additional consistencies not checked in the foregoing analysis, such as intensity ratios between lines or lines and continuum, etc. A complete correspondence between calculated and time-integrated spectra is not expected unless most of the spectrum is emitted over time and space where the conditions do not change significantly. This can be expected to approximately be the case for emission from peak compression. Figure 55.12 shows the *RATION* spectrum corresponding to $T = 1$ keV and $N_e = 0.7 \times 10^{24}$ cm^{-3} ($\rho = 2.3$ g cm^{-3}). The effect of opacity was included, assuming a 40-μm-diam core. Also, an instrumental linewidth of 15 eV was included in the calculation. The predicted spectrum agrees with the measured spectrum in general, but not in all details. For example, the line-intensity ratios are somewhat different and indicate that the temperature in the experiment as measured by the line ratios is lower than 1 keV. The difference in T_e as determined by the lines and by the continuum is the result of integrating in time and space over emission from somewhat different temperatures.
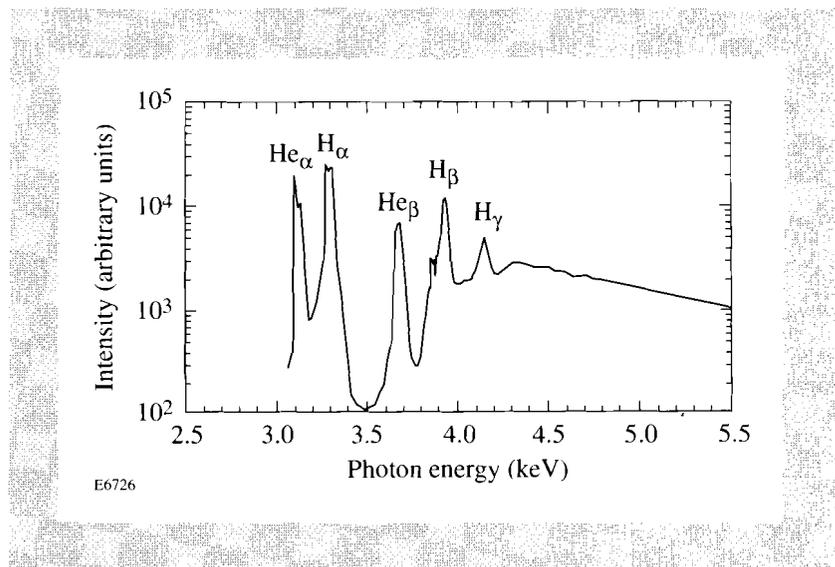

E6726

Fig. 55.12
The spectrum calculated by the code *RATION* with the following assumed parameters: $T = 1$ keV and $N_e = 0.7 \times 10^{24}$ cm^{-3} ($\rho = 2.3$ g cm^{-3}).

High-Pressure Argon Experiments

In Fig. 55.13 we show a comparison between the spectra from a high-pressure (shot 24498) and a low-pressure (shot 24501) argon target. As mentioned above, the high or low pressure refers here to the partial pressure of argon. This difference in pressure affects the resonant (self) absorption of argon lines and yields very different emergent spectra.

One issue needing clarification before analysis can be applied is the emission from the argon gas trapped in the polymer shell during the filling process. This gas is heated by the laser and emits argon lines from the ablated region. As such, it is not relevant to the diagnosis of the compressed core. However, these lines provide convenient spectral references because their broadening in the low-density ablated plasma is very small. Figure 55.13 shows that these narrow lines appear only in the high-pressure shot; the low-pressure shot shows Stark-broadened lines coming from the compressed core. This can be understood by the severe opacity of the argon lines in the high-pressure case. The lines from the core are absorbed on the way out within a cooler argon layer, and the narrow lines from the shell can be observed with no competition from the core lines. In the low-pressure case, the unabsorbed core lines dominate over the lines from the shell because the core argon gas has both higher total mass and higher density as compared to the argon gas in the shell. On the other hand, the intensity of the argon lines from the shell should be proportional to the fill pressure, which is consistent with Fig. 55.13.
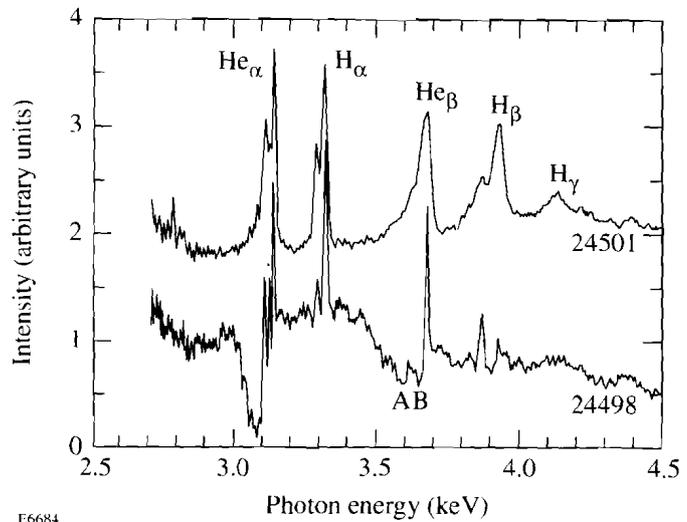

Fig. 55.13
Measured spectra at low and high argon-fill pressures. For shot 24501, the target was filled with 0.1 atm argon and 20 atm deuterium; for shot 24498 the target was filled with 20 atm argon. The scale on the left refers to shot 24498; the spectrum for shot 24501 is on the same intensity scale but was displaced upward for clarity. The A and B features are explained in the text.

The high-pressure spectrum shows no lines of helium-like (Ar^{+16}) nor hydrogen-like (Ar^{+17}) species from the core, as is the case for the low-pressure shots. The absence of these lines cannot be attributed solely to self-absorption (opacity) because under strong opacity conditions these lines should have appeared as absorption lines. This is indeed the case for lines of lower ionizations as seen in the high-pressure spectrum. There are two groups of such lines that appear in absorption. The first is on the low-energy side of the helium-α line $(1s2p-1s^2)$ at 3140 eV. The second appears on the low-energy side of the helium-β line $(1s3p-1s^2)$ at 3683 eV. Whereas the first group has been studied extensively in the past,[8-14] the second group has been studied only recently[15] and has been observed only in emission.[16] The absorption lines in the first group are due to transitions of the type $1s^2-1s2p$ in argon ions with partially filled L shells; likewise, the absorption lines in the second group are due to transitions of the type $1s^2-1s3p$, $1s3d$ in argon ions with partially filled L shells. These lines are thus absorbed in a cooler argon peripheral layer, where lower ionizations prevail. The area enclosed within these absorption lines is proportional to the $\rho\Delta R$ of that cooler region.[8] However, in typical cases the first group of absorption features (near the helium-α line) has yielded only a lower limit on that quantity. The reason is that a relatively small value of $\rho\Delta R$ is sufficient to absorb these lines almost completely. In Ref. 8, the flat-bottom absorption structure near the helium-α line yielded a lower bound of only ~5 mg/cm^2 for the $\rho\Delta R$ of the cool, absorbing layer.

The interest in the absorption features near the helium-β line is that their absorption probabilities are lower than for the comparable absorption lines near the helium-α line. As a result, the absorption near the helium-β line in Fig. 55.13 is much weaker than that near the helium-α line. The former can thus yield a better estimate of the $\rho\Delta R$ of the absorbing layer. Using the methods described in Ref. 8, we estimate for the $\rho\Delta R$ of the absorbing layer of Fig. 55.13, using the absorption features near the helium-α line: $\rho\Delta R > 5$ mg/cm^2. Applying the same procedure to the absorption features near the helium-β line we obtain $\rho\Delta R \sim 8$ mg/cm^2. In deriving this value we made use of the absorption oscillator strength in 1s–3p transitions in hydrogen-like ions, which is 5.4 times lower than for 1s–2p transitions. As in Ref. 8, the $\rho\Delta R$ of the absorption layer consists of the sum of absorption due to successive charge states, which is proportional to the total area within the absorption structure.

The spectral features near the helium-β line have been recently measured in emission (rather than in absorption) and extensively studied. A comparison of the spectra in the two cases shows a close similarity. In particular, the two features marked A and B in Fig. 55.13 correspond to the two features calculated in Ref. 15 as due to transitions of the type A: $1s2l3l' - 1s^2 2l$, and type B: $1s3l3l' - 1s^2 3l$. We note that in type A the "spectator" electron is in the $n = 2$ shell, whereas in type B it is in the $n = 3$ shell. When the lines appear in absorption, the absorbing (or initial) state in type A is the ground state of the relevant ion, whereas in type B it is an excited state. The fact that the A and B features in Fig. 55.13 have comparable areas indicates strong excitation of the absorbing ions. The excitation energy of the various ions contributing to the absorption varies from 200 eV for the lithium-like ion to 250 eV for the nitrogen-like ion.

Using these values in a collisional-radiative model, we estimate the temperature in the absorption region to vary in the range 80 to 160 eV. Other inner layers of argon fill gas can have a higher temperature; however, for much higher temperatures the population would have been dominated by helium-like ions. We know this is not the case since no helium-like absorption lines appear in the high-pressure spectrum of Fig. 55.13. Using this, we can obtain an upper limit on the temperature in the absorption layer: $T < 600$ eV.

It is instructive to compare the high-pressure spectrum of Fig. 55.13 to code prediction. Figure 55.14 shows the spectrum calculated by the *LILAC* code coupled to an atomic physics post-processor. Here, strong absorption in helium-like lines is evident, contrary to the observed spectrum. It should be noted that the absorption features near the helium-β line are not included in the code calculations, as are the absorption features near the helium-α line. In particular, the predicted strong absorption of the He$_\beta$ line (at 3683 eV) is missing in the observed spectrum. The narrower He$_\alpha$ line (at 3140 eV) overlaps the nearby lower-ionization absorption features, so it is not very clear whether the line is missing from the high-pressure spectrum. However, the much broader He$_\beta$ line (especially its higher-frequency wing) is free from such overlap, and its absence from the measured spectrum is thus more definite. If the core temperature is nowhere higher than about 600 eV, no strong Ar^{+16} lines would be emitted; however, these very lines could still appear in absorption due to continuum absorption on Ar^{+16} transitions. The absence of such absorption lines can be explained by a combination of two factors: (a) cooler-than-predicted temperature and (b) lower-than-predicted $\rho\Delta R$ for the absorption region and, by implication, for the whole core. The lower-than-predicted values could be the result of hydrodynamic instability, which degrades the compression and, thus, its resulting core heating.
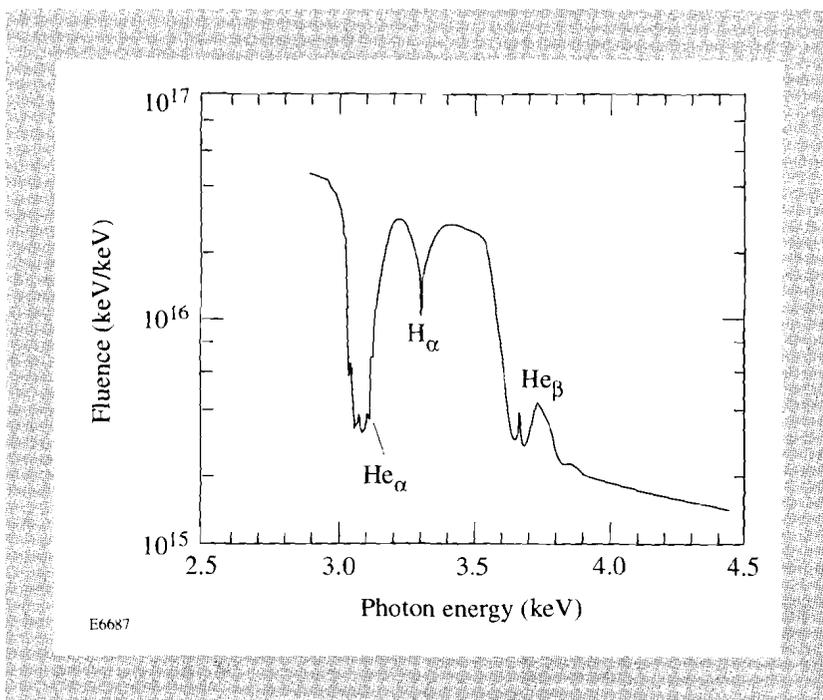

E6687

Fig. 55.14
Time-integrated, code-predicted spectrum for shot 24498 (compare to Fig. 55.13).

ACKNOWLEDGMENT

REFERENCES

1. C. F. Hooper (private communication).

2. H. R. Griem, *Spectral Line Broadening by Plasmas* (Academic Press, New York, 1974), Eq. (16), p. 8.

3. J. C. Stewart and K. D. Pyatt, Jr., Astrophys. J. **144**, 1203 (1966).

4. H. R. Griem, *Plasma Spectroscopy* (McGraw-Hill, New York, 1964), Chap. 13.

5. *ibid*, Chap. 5.

6. R. Epstein, S. Skupsky, and J. Delettrez, J. Quant. Spectros. Radiat. Transfer **35**, 131 (1986).

7. R. W. Lee (private communication).

8. LLE Review **49**, 1 (1991).

9. J. Delettrez, R. Epstein, D. K. Bradley, P. A. Jaanimagi, R. C. Mancini, and C. F. Hooper, Jr., in the *Proceedings of the International Workshop on Radiation Properties of Hot Dense Matter*, Sarasota, FL, 22–26 October 1990, p. 309.

10. L. A. Woltz, V. L. Jacobs, C. F. Hooper, Jr., and R. C. Mancini, Phys. Rev. A **44**, 1281 (1991).

11. R. Epstein, Phys. Rev. A **43**, 961 (1991).

12. R. C. Mancini, C. F. Hooper, Jr., J. A. Delettrez, R. Epstein, D. K. Bradley, P. A. Jaanimagi, and M. C. Richardson, in the *Proceedings of the International Workshop on Radiation Properties of Hot Dense Matter*, Sarasota, FL, 22–26 October 1990, p. 82.

13. R. C. Mancini and C. F. Hooper, Jr., Rev. Sci. Instrum. **61**, 27 (1990).

14. R. C. Mancini, C. F. Hooper, Jr., and R. L. Coldwell, to be published in Journal of Quantitative Spectroscopy & Radiative Transfer.

15. R. C. Mancini *et al.*, Rev. Sci. Instrum. **63**, 5119 (1992).

16. B. A. Hammel *et al.*, Rev. Sci. Instrum. **63**, 5017 (1992).